Journal of Materials Chemistry A

ROYAL SOCIETY OF CHEMISTRY

PAPER

View Article Online
View Journal

Cite this: DOI: 10.1039/d5ta10405j

Carbon monoxide ligation at single metal atom sites in a 2D manganese-cobalt coordination network: equilibrium at room temperature

Michela De Col, †[a] Danilo Comini, †[a] Stefania Baronio,†[a] Basant Roondhe,[b] Alessandro Namar,[a] Davide Bidoggia,[a] Mattia Scardamaglia,[c] Paolo Giannozzi *[bd] and Erik Vesselli *[aef]

We find that CO ligates selectively to nitrogen tetra-coordinated Co(I) single metal atom sites at room temperature in a manganese–cobalt bi-metallic coordination network self-assembled on graphene. The bound state is metastable, determined by pressure-dependent equilibrium conditions between adsorption and desorption, with an upright, end-on bonding geometry (binding energy 0.73 eV). The ligand vibrational hot-band can be populated due to the weak coupling with the substrate. The CO uptake/saturation curve is modeled using Temkin and Hill isotherms, unveiling network-mediated anti-cooperative adsorption. While contributions from direct dipole–dipole interactions and Förster energy transfer are ruled out, the observed anti-cooperativity originates from network-mediated electronic and magnetic effects. Our findings provide direct insight into ligand dynamics at single metal atom sites in 2D materials and suggest tunable reactivity properties of a 2D biomimetic functional material through its tailored design.

Received 22nd December 2025
Accepted 12th March 2026

DOI: 10.1039/d5ta10405j

rsc.li/materials-a

Introduction

The adsorption of carbon monoxide (CO) at surfaces has been a central topic in surface science since the early days of ultra-high vacuum (UHV) studies.[1] Over the decades, research has aimed to achieve a deep understanding of adsorption and bond formation processes, with the goal of developing novel model catalysts for more efficient and selective catalytic reactions involving CO. Both single crystal metal surfaces and supported metal nanoclusters[2–4] have been adopted as optimal model systems offering multiple possible coordination sites and a variety of available electronic states for bond formation with carbon monoxide, with a more recent extension to the case of single metal atom sites.[5] Combined multi-technique experimental and theoretical/computational approaches have led to a deep comprehension of the CO–metal atom bond, with the generally most stable configuration identified as the terminal (on-top) carbon-coordinated bonding geometry. Carbon monoxide is generally accepted as an optimal molecular probe to investigate the properties of adsorption (surface science) and ligation (biochemistry) sites. With the more recent introduction of ambient-pressure surface science experimental methods like *e.g.* Ambient Pressure X-ray Photoelectron Spectroscopy (AP-XPS), Infrared-Visible Sum-Frequency Generation Spectroscopy (IR-Vis SFG), and Polarization-Modulation Infrared Reflection Absorption Spectroscopy (PM-IRRAS), the role of density-dependent lateral interactions in surface CO layers has been deeply addressed, providing insight into both direct (dipole) and indirect (surface-mediated) interaction mechanisms.[6–10] In parallel, laser-assisted pump-probe out of equilibrium investigations provided information about the role of excited states and electron–phonon mediated adsorption, diffusion, reaction, and desorption processes down to the fs time resolution.[11–15] Mechanic probes (STM, AFM) initially contributed with real-space imaging of the bonding geometries and, more recently, single-molecule manipulation gave access to transport mechanisms mediated by tunneling and isomerization effects.[16–19]

Carbon monoxide is also exploited in biochemistry for the investigation of the geometric, electronic, and chemical reactivity properties of single metal atom sites embedded in organic pockets in proteins and specific enzymes, with particular reference to tetra-coordinated porphyrin cages.[20–22] The use of CO as a probe molecule has then been further extended to single-metal atom sites up to near-ambient pressure conditions

[a]*Department of Physics, University of Trieste* via *A. Valerio 2, Trieste 34127, Italy. E-mail: evesselli@units.it*

[b]*Department of Mathematics, Computer Science, and Physics, University of Udine, Udine, I-33100, Italy. E-mail: paolo.giannozzi@uniud.it*

[c]*MAX IV Laboratory, Lund University, Lund, 22100, Sweden*

[d]*CNR – Istituto Officina dei Materiali, SISSA, Trieste 34136, Italy*

[e]*CNR – Istituto Officina dei Materiali (IOM), S.S. 14 km 163.5, Area Science Park, Basovizza, Trieste 34149, Italy*

[f]*Center for Energy, Environment and Transport Giacomo Ciamician, University of Trieste, Trieste 34127, Italy*

† These authors contributed equally to the experiments.

in 2D biomimetic organic networks supported at surfaces,[23–25] evidencing emergent properties originating from the cooperative interplay of the self-assembled coordinating molecular tectons.[26,27] Electronic, geometric, and magnetic effects, together with electron–phonon coupling mechanisms, were found to contribute to the appearance of interesting novel properties affecting the CO ligand. In our previous studies we reported long-lived excitons generated by impinging visible light that, according to coherent singlet-fission mechanisms, affect the vibronic properties of the layer at room temperature and ambient pressure conditions.[23] We also observed vibrational excited states, namely hot bands, deviations from Langmuir isotherms due to coverage–dependent interactions,[26] and specific, tunable reactivity properties of the embedded single metal atoms.[28] In this framework, these 2D coordination networks act as biomimetic systems by reproducing the local coordination environment of single metal atoms in natural proteins, including the square-planar nitrogen tetracoordination and the axial 'surface *trans*-effect' provided here by the graphene support.[29]

Within this stream, we report here a combined experimental and computational study of the interaction of carbon monoxide at room temperature, from UHV up to ambient pressure conditions, with a M_1TPyP–M_2 coordination network supported by graphene (Gr). A single layer of manganese (M_1 = Mn) tetrapyridyl-porphyrins (TPyP) was indeed found to self-assemble on Ir(111)-supported Gr into an ordered network with close-to square symmetry when coordinating M_2 = Co atoms at the peripheral nitrogen terminations of the pyridinic residues (Fig. S1).[30] We show that the latter Co(I) single atom sites offer coordination to carbon monoxide, which ligates in a metastable configuration at room temperature due to the relatively low Co–CO binding energy. Equilibrium conditions with a CO background yield a pressure-dependent population of the Co sites, with saturation occurring above 10^{-3} mbar. The weak molecule-support and lateral interactions allow population of the vibrational hot-band for the internal C–O stretch mode upon illumination of the layer with infrared radiation and account for the observed anti-cooperative mechanism driving the uptake process, despite the large lateral distance (>1.5 nm) between the nearest neighbor ligation sites.

Methods

Experimental methods

Sample preparation. The Ir(111) surface was cleaned by standard methods, following repeated sputtering and annealing cycles (Ar^+, 2 keV, 1275–1375 K), alternated with exposure to 5×10^{-8} mbar O_2. A single Gr layer was grown by thermal decomposition of C_2H_4. The clean Ir sample was heated ($T > 1275$ K) and exposed to a C_2H_4 background (5×10^{-8} mbar) for 2 minutes. The gas pressure was then increased (up to 3×10^{-7} mbar), and finally the temperature was lowered while recovering ultra-high vacuum (UHV) conditions. Depending on the specific experimental setup, the quality of the Gr sheet was checked with LEED, XPS, or IR-Vis SFG. Mn(III) meso-tetra (4-pyridyl) porphin chloride molecules (Frontier Scientific) were outgassed at 470–525 K for several hours in a crucible in UHV to remove gas contaminants and organic residues. The Cl atom ligated to the central metal stabilizes the complex as Mn(III), and is thermally detached from the porphyrins when they are heated, resulting in a reduction of the metal center to Mn(II).[31–35] Absence of Cl in the deposited layer was verified by XPS. The sublimation temperature varied in the 650–680 K range according to the crucible-sample distance, achieving deposition rates of approximately 0.06 ML min^{-1}, in order to grow a full monolayer (ML) in about 15–20 minutes. The sample was kept at 473 K during the growth to promote ordering without affecting stability. The maximum achieved molecular surface coverage was kept below 1 ML to avoid kinetic hindrance in the reordering process upon Co post-coordination as well as the formation of a second layer. The bi-metallic heterostructure was obtained by physical vapor post-deposition (PVD) of Co ad-atoms on the MnTPyP/Gr/Ir(111) layer by resistively heating a Co filament (250 μm diameter). In this manuscript, the Co coverage will be expressed referring to a porphyrin monolayer, so that 1 ML Co corresponds to one Co ad-atom for each molecule in 1 ML MnTPyP, in analogy with our recent work.[30,36,37] In general, Co was dosed to achieve a Co : MnTPyP ratio lower than 1, to avoid formation of Co clusters due to excess Co.[30,36,37] The evaporation rates were calibrated either by Auger electron spectroscopy (AES) or XPS, depending on the available method. This approach overcomes the extreme challenges posed by the low surface density of active sites (~1% ML) and the limitations of conventional spectroscopic methods, representing a state-of-the-art advancement in 2D material characterization.

Sum-frequency generation spectroscopy. Infrared–Visible Sum-Frequency Generation (IR–Vis SFG)[38,39] vibronic spectroscopy measurements were performed in a dedicated setup at the Department of Physics of the University of Trieste, best described elsewhere.[40] Briefly, a UHV system with a base pressure of 5×10^{-11} mbar hosts standard surface science preparation and characterization techniques and is directly coupled with a high-pressure cell for *in situ* IR–Vis SFG spectroscopy. The laser beams enter and exit the cell through UHV-compatible BaF_2 windows. The excitation source (Ekspla, 1064 nm, 30 ps, 50 Hz) delivers a 532 nm (2.33 eV) visible beam, and tunable IR radiation in the 1000–4500 cm^{-1} range with an energy of 100–300 μJ per pulse, depending on the wavelength. All measurements were performed at room temperature. The raw SFG spectra were normalized to the impinging infrared and visible excitation intensities, and to a reference signal from clean Au to account for the energy-dependent IR intensity and the time-dependent intensity fluctuations of the sources. Normalized SFG spectra were analyzed using least-squares fitting to the widely adopted parametric, effective expression of the nonlinear second-order susceptibility.[38] Further details and examples can be found in our previous works.[28,40,41] In summary, by modeling the observed lineshapes, accounting for the resonant IR–Vis vibronic transitions and for the non-resonant background, we describe all the interference terms associated with the relative phases, and consider the Lorentzian broadening typical of a stimulated spectroscopic transition and related to the

dephasing rate, which in turn stems from the excited-state lifetime and the elastic dephasing of the vibronic state.[42] In the figures, we plot the normalized IR–Vis SFG signal intensity (markers), together with the best fit (lines) and the resonances, each including interference with the non-resonant background (color-filled profiles). The latter are calculated with the parameters obtained from the fitting procedure following the literature,[40] choosing one of the possible multiplet solutions associated with the non-unicity of the parameter sets.[43] In the present study, spectra were collected in both ppp and ssp polarization configurations (sfg-vis-ir).

Ambient-pressure X-ray photoelectron spectroscopy. AP-XPS experiments were performed at the HIPPIE beamline of the MAX IV synchrotron radiation facility in Lund (S), allowing also for *in situ* and *operando* measurements at the surface–gas interface.[44] A slow raster-scan of 0.5 μm s^{-1} was set up to prevent beam-induced degradation of the sample during the measurements. Mn and Co $2p_{3/2}$ core level spectra were acquired upon excitation with 1000 eV photons, O 1s with 750 eV, N 1s with 514 eV, C 1s and Ir $4f_{7/2}$ with 400 eV photons, respectively, to optimize photoionization cross section and surface sensitivity. The binding energy scale was calibrated with respect to the Fermi level. The XPS spectra were best fitted by least squares fitting methods according to the Doniach-Šunjić or Voigt lineshapes,[45] depending on the core level metallicity, after subtraction of a linear background or a polynomial function previously optimized on the clean sample reference background.

Computational methods

Density functional theory (DFT) calculations were performed using the plane-wave pseudopotential formalism implemented in the Quantum ESPRESSO package.[46,47] Slab models were constructed with periodic boundary conditions and a supercell height of 20 Å, ensuring a vacuum gap of at least 15 Å between periodic replicas along the surface normal. The Ir(111) support beneath Gr was omitted, as earlier studies have shown its effect on the overlayer to be negligible.[37,48] For the MnTPyP–Co/Gr system, an oblique surface cell was employed with lattice vectors $a = 28.36$ Å, $b = 20.23$ Å and in-plane angle $\alpha = 135.1°$. Each cell contained two MnTPyP–Co molecules positioned 3 Å above a Gr sheet of 70 hexagons. The small lattice mismatch induced a slight distortion in the Gr, giving in-plane lengths of 2.48 Å and 2.53 Å and an inter-vector angle $\gamma = 118.7°$. Spin-polarized calculations used the Perdew–Burke–Ernzerhof (PBE) functional within the generalized gradient approximation (GGA).[49] On-site Coulomb interactions (DFT + U) for Mn and Co 3d states were included *via* the self-consistent linear-response approach,[50] with U(Mn) = 3.2 eV and U(Co) = 6.12 eV. Long-range dispersion forces were described using Grimme's D3 correction.[51] Core-valence interactions were modelled with Vanderbilt ultrasoft pseudopotentials.[52,53] Wavefunction and charge-density cut-offs were set to 60 and 240 Ry, respectively. Electronic occupations were treated with Methfessel–Paxton smearing ($\sigma = 0.01$ Ry).[54] Geometry optimization was carried out using the Broyden–Fletcher–Goldfarb–Shanno (BFGS) quasi-Newton algorithm,[55] with convergence criteria of 1×10^{-6} Ry for total energy and 1×10^{-3} a.u. for forces. Brillouin-zone sampling used a $2 \times 4 \times 1$ Monkhorst–Pack grid for self-consistent (SCF), and a $4 \times 8 \times 1$ grid for non-self-consistent calculations.[56] Charge-transfer was evaluated using Bader analysis.[57,58] Charge-density difference maps were obtained by subtracting the densities of the isolated components from that of the combined system.

Results and discussion

Fig. 1 (bottom row) plots a selection of the core level spectra collected at room temperature in UHV of the pristine, as prepared, MnTPyP–Co/Gr layer. We focus on the single metal atoms (Co $2p_{3/2}$ and Mn $2p_{3/2}$, panels a and b, respectively) and on oxygen (panel c). In agreement with our previous characterization,[30] the spectral features indicate the presence of Mn(III) and Co(I) species. In the Co $2p_{3/2}$ spectrum, we could resolve four components at 778.5, 780.0, 781.6, and 784.7 eV. The lowest binding energy feature is associated with a Gunnarsson–Schönhammer screening effect, with the two central peaks originating from multiplet splitting and the fourth, highest energy peak being a non-adiabatic satellite. Similarly, the manganese spectrum is also strongly affected by multiple splitting due to final state effects. We could resolve four components at 641.0, 642.3, 643.8, and 647.3 eV. Following a thorough and clean preparation recipe in UHV, as indicated in the methods section, no oxygen contamination could be detected on the pristine layer (panel c). Introduction of a static carbon monoxide background at room temperature ($p_{CO} = 2 \times 10^{-2}$ mbar) clearly yields ligation of CO, observable thanks to a stationary adsorption–desorption equilibrium, with two dominant spectral components growing in the O 1s spectrum (panel c), accompanied by a low binding energy shoulder. The most prominent peak (534.1 eV) is associated with the upright CO molecule adsorbed on-top of a single metal atom with carbon coordination, while the high energy peak at 538.5 eV is assigned to gas phase carbon monoxide.[59,60] The small binding energy shoulder at 532.7 eV is attributed to atomic oxygen contamination of the layer and/or of the graphene support,[61] occurring upon spillover from the reactive metal sites of low concentrations of water/oxygen contaminants or originating from CO dissociation at defective sites.[36] Assuming saturation of the Co sites by CO, it can be estimated that this contamination amounts to less than 1‰ ML. The spectroscopic picture obtained from the analysis of the O 1s core level is also supported by the corresponding C 1s counterpart (Fig. S2). In addition to the graphene and porphyrin components of the pristine layer at low binding energy,[30] a peak due to ligated CO is observed at 286.4 eV in the CO ambient pressure measurements. Compatibly, on-top (terminal), strong CO chemisorption at Co single crystal metal surfaces yields C and O 1s core level binding energies around 286.2–286.3 and 532.2–532.5 eV, respectively,[62,63] and similar values are observed for adsorption on Mn.[59] O 1s binding energy values up to 534.1 eV have been observed for weakly bound terminal species, instead.[64] Coming to the identification of the metal species active towards CO

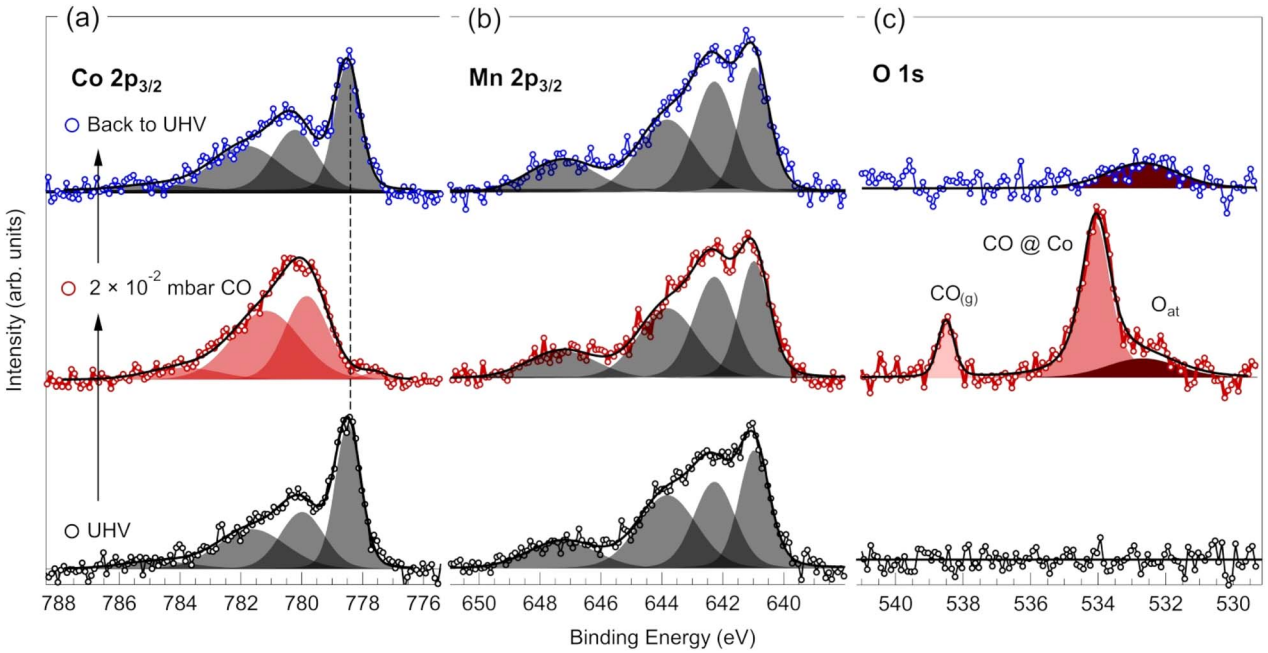

Fig. 1 Synchrotron radiation XPS spectra of the (a) Co $2p_{3/2}$, (b) Mn $2p_{3/2}$, and (c) O 1s core levels of the MnTPyP–Co/Gr layer collected at room temperature in UHV (bottom row), at equilibrium in 2×10^{-2} mbar CO (central row), and after recovering UHV conditions (top row). Photon energies were 1000 and 750 eV for Co, Mn, and for O core levels, respectively.

ligation in our case, the answer is quite straightforward. When looking at the Co and Mn spectra (panels a and b, respectively), we notice that, while the latter species is completely unaffected, the Co spectrum is strongly modified, indicating that carbonylation of cobalt is taking place. The most evident effect is the quenching of the Gunnarsson–Schönhammer component, indicating suppression of the charge transfer mechanism that was responsible for that feature in the UHV case. The multiplet splitting components undergo a mild redshift by 0.2–0.4 eV, with the shake-up satellite moving to 0.8 eV lower energy. Similarly, CO ligates to the pyridinic Co sites also in the case of the twin CoTPyP–Co system, a result that was also supported by *ab initio* computational methods.[37] That finding was easily explained by looking at the calculated density of states projected on the Co $3d_z^2$ and $3d_{zx,zy}$ orbitals, involved in CO ligation, on both the nonequivalent Co sites. For the peripheral Co, the Blyholder model that describes CO ligation on metals applies,[65,66] as the CO σ can donate electrons to the Co $3d_z^2$, while the CO π* accepts electrons from the Co $3d_{zx,zy}$.[37] Instead, hybridization is less effective on the metal atom located inside the porphyrin macrocycle, as its orbitals are already involved in the bonding with the iminic N atoms.[37] A similar picture also applies here for the MnTPyP–Co case.

Horizontal adsorption of CO at the Co sites is found to be unstable, with optimization ending in a stable, nearly vertical (Fig. 2a), end-on geometry (C-bonded), in agreement with the experimental observations. Upon ligation, the internal C–O bond length increases from 1.12 to 1.16 Å (+3.6%) with an adsorption energy of 0.97 eV. The calculated projected density of states (PDOS) is shown in Fig. 2b. Hybridization between the Co d_z^2 and CO π* states is evident in the PDOS (Fig. 2b), while the Mn center acts as an electronic 'buffer' that regulates the π-backdonation available at the peripheral sites. In addition to the CO states, the Co $3d_z^2$ and $3d_{zx,zy}$ are the only orbitals involved in the bonding. For best clarity, we plot in the figure both the case of the pristine layer (left) and of CO ligation (right). In the former case, bonding states are observed at −3.5 and −2 eV corresponding to $3d_z^2$ and $3d_{zx,zy}$, respectively. Above the Fermi level, set as the zero reference, antibonding states at +1 eV originate from the overlapping contributions from the N $2p_z$ and the same Co $3d_z^2$ and $3d_{zx,zy}$. The Co $3d_{zx,zy}$ level splits at −3.5 and −4.5 eV by overlapping with the out-of-plane N $2p_z$, arising from the saddle-shaped distortion of the macrocycle, which renders the two pairs of iminic N atoms inequivalent. Upon CO ligation, the average Co–N bond length increases to 2.293 Å, consistent with *a* +1 oxidation state of the metal atom.[67] This bond length clearly differs from the shorter Co–N distances typically associated with +2 (≈2.2 Å) and +3 (≈1.9 Å) oxidation states. We quantified the oxidation state of the Co metal atom using the technique reported in the literature.[58] The orbital occupation values are reported in Table S1. Magnetic communication between the central Mn^{3+} and peripheral Co^{1+} sites occurs *via* superexchange interaction through the nitrogen-bridged frame. CO ligation, acting as a strong-field ligand, modifies the Co d-orbital occupancy and shifts the spin-state balance of the network. This is explicitly supported by the hybridization between the Co d_z^2 and CO π* states observed in the PDOS (Fig. 2b). We have also calculated the charge transfer between the CO and the MnTPyP–Co/Gr layer using Bader charge analysis. The Charge Density Difference (CDD) map in Fig. 2c illustrates the physical basis of this interaction, showing a clear electron accumulation (yellow) on the CO ligand and

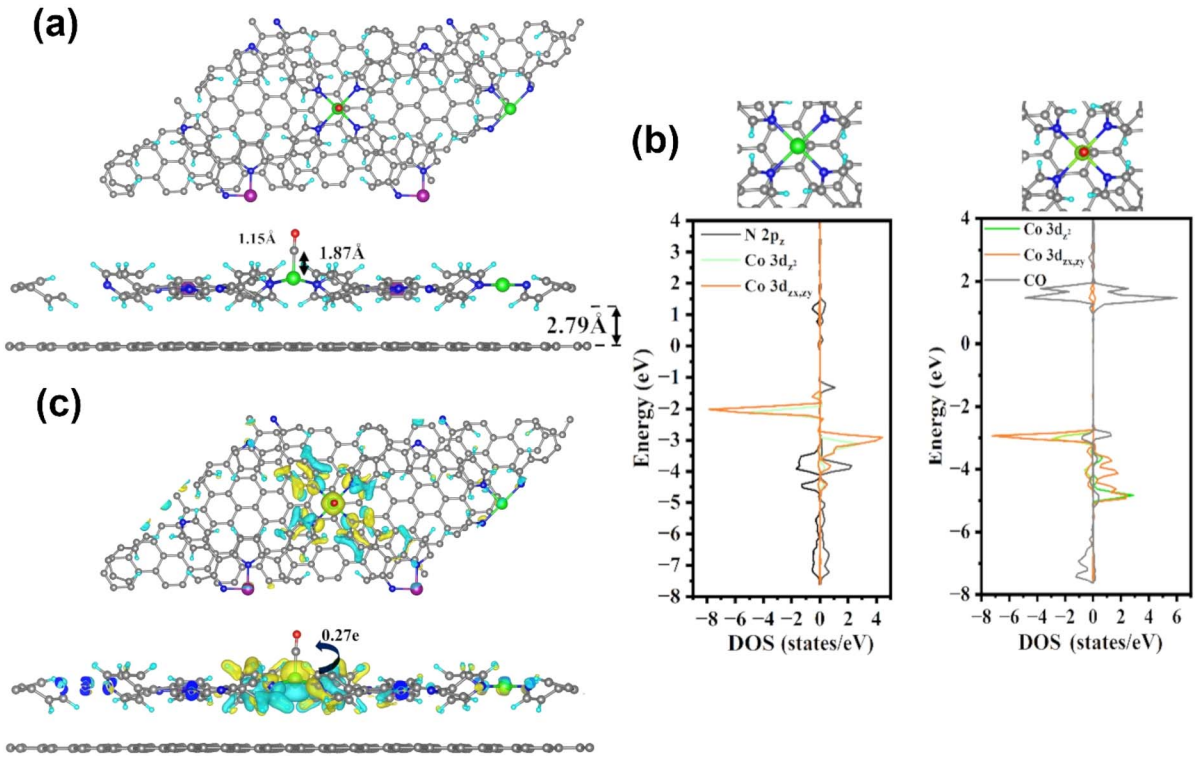

Fig. 2 (a) Optimized geometry of the CO@Co in the MnTPyP–Co/Gr system, with Co coordinated at the pyridinic site. Key structural parameters include a Co–CO bond length of ~1.87 Å and an elongated internal C–O bond of ~1.15 Å, indicating partial activation of the CO molecule; (b) density of states (DOS) projected onto the Co d-orbitals and CO molecular orbitals before (left) and after (right) ligation, showing hybridization between Co d_z^2 and CO π* states near the Fermi level, as well as shifts in the CO 5σ state, consistent with σ-donation and π-backdonation; (c) charge density difference plot, with yellow and cyan isosurfaces representing electron accumulation and depletion, respectively, highlighting a net charge transfer of ~0.27 e^- to the CO ligand, involving the Co center and the coordinated pyridinic moieties.

a corresponding depletion (cyan) at the Co center. CO ligation is accompanied by a net charge transfer of approximately 0.27 e^- to the CO molecule, involving the pyridinic moieties of the adjacent coordinating porphyrins in the charge redistribution process. Locally, this suggests formation of a donor–acceptor interaction, where electron density from the Co d-orbitals is donated into the empty π* antibonding orbitals of CO (σ-donation), accompanied by a weaker back-donation from the filled CO 5σ orbital into the Co d orbitals, in agreement with the Blyholder model.[68] This redistribution strengthens the Co–C bond and slightly weakens the C–O bond, a characteristic signature of metal–CO coordination.

Carbon monoxide adsorption has also been widely studied by vibrational spectroscopic techniques, adopting a large variety of spectroscopic approaches. The C–O stretching band of CO adsorbed on-top is generally observed above 1800 cm^{-1} and up to 2120 cm^{-1} on metal surfaces, clusters, single metal atoms, and metal–organic molecules,[4,10,23,37,69–72] with the gas-phase value at 2143 cm^{-1}.[73] Upon exposure of the MnTPyP–Co/Gr system to a CO background, in addition to the characteristic vibronic fingerprints of the layer (Fig. S3), by means of IR-Vis SFG spectroscopy we observe the pressure-dependent growth of two additional vibrational resonances (1968 and 1942 cm^{-1}) in the C–O internal stretch energy region due to terminal CO ligation at the Co sites (Fig. 3). The two features are observable in both ppp and ssp polarization combinations (panels a and b of the figure) and reversibly disappear upon recovering UHV conditions (Fig. S4), in agreement with the corresponding C and O 1s XPS core levels discussed above. The wavenumber separation of 26 cm^{-1} corresponds to about 3 meV in energy. We associate the two newly observed vibronic features with the fundamental (low wavenumber) and the hot-band (high wavenumber) excitations of the internal stretching mode of the CO ligand,[37,74,75] based on the following reasoning. In general, the presence of multiple resonances corresponding to the same chemical species can be associated with non-equivalent adsorption sites or geometries,[4,71] yielding however chemical shifts larger than the one we observe. Carbon monoxide adsorbed at (contaminant) Co clusters on graphene would instead contribute at >2000 cm^{-1},[10,26,69,70,76] thus we can rule out this case as well. We observed a faint and broad peak associated with such species in 10^{-3} mbar CO only after excess Co evaporation (MnTPyP : Co = 0.6 : 1) around 2000 cm^{-1} (Fig. S5) where, interestingly, the resonances shape and ratio are also considerably modified, with an almost quenched fundamental peak. Excitonic mechanisms could also, in principle, account for the observed vibronic splitting, but generally yield much smaller shifts.[23] Finally, multiple vibrational excitations can lead to the splitting of a resonance into distinct components.[37,74,75] The latter phenomenon can be easily visualized by considering

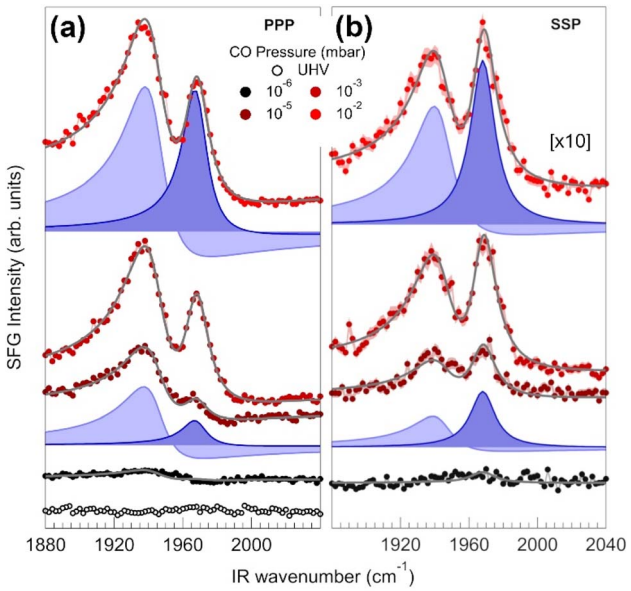

Fig. 3 IR-Vis SFG spectra of the energy region that is specifically diagnostic of the internal stretch of the CO ligand. Both ppp (a) and ssp (b) polarization combinations were adopted. Starting from the bottom spectrum of the pristine MnTPyP–Co/Gr layer in UHV, the background pressure of carbon monoxide was stepwise increased up to saturation. The normalized data (dots) are shown together with the best fit (continuous, gray line) and the associated resonances (filled profiles) obtained from the modeling of the second order susceptibility described in the methods section.

adsorbed CO molecules as localized oscillators, with an anharmonic interatomic potential.[74] The energy separation between consecutive vibrational excited states gradually decreases, thus a resonance originated by the $\nu \rightarrow \nu + 1$ transition will have progressively lower energy as ν increases.[75] The anharmonic frequency shift of the hot-band reported for CO adsorbed on CoTPyP–Co,[26] Ir(111),[74] and Ru(0001)[75] is of the order of a few tens of cm^{-1}, in agreement with our results. Thus, we associate the 1968 cm^{-1} resonance to the $0 \rightarrow 1$ transition ($\omega_{0\rightarrow1}$, $\nu = 0$) and the one at 1942 cm^{-1} to the $1 \rightarrow 2$ excitation ($\omega_{1\rightarrow2}$, $\nu = 1$). If we assume the C–O interatomic potential to be a Morse potential, the anharmonicity constant χ_e can be calculated according to:

$$\chi_e = \frac{\omega_{0\rightarrow1} - \omega_{1\rightarrow2}}{2\omega_{0\rightarrow1}}$$

If the energies of the $\omega_{0\rightarrow1}$ and $\omega_{1\rightarrow2}$ resonances are known.[75] In our case we get $\chi_e = (6.66 \pm 0.08) \times 10^{-3}$, similarly to CO/Ir(111),[74] and to CO/CoTPyP–Co/Gr/Ir(111),[26] for which values of 0.0065 and 0.0061 were measured, respectively, with the latter being identical to the gas phase value (0.0061).[77,78] Concerning the fundamental and hot-band resonances amplitude ratio, we find that it depends on the intensity of the impinging IR beam. According to the SFG process, the resonant amplitude is proportional to the population difference between initial and final states, which in turn depends on the intensity of the impinging IR beam for the vibrational part of the transition, thus explaining the observed behavior and further supporting the interpretative picture. Another factor to be considered is that the $\nu = 1 \rightarrow 2$ transition has a higher dynamic dipole moment, associated with a more intense resonant signal.[74]

At variance with XPS, the extreme surface sensitivity of IR-Vis SFG allows us to finely investigate the adsorption process *in situ* as a function of progressively increasing pressure, from UHV to saturation (mind that saturation corresponds to about 1% ML in terms of absolute coverage of the available Co sites). Hence, the coverage dependence of the CO–Co interaction energy can be measured, together with a quantitative investigation of the kinetics (cooperativity effects) and of the anharmonicity of the CO interatomic potential, which is related to the dissociation energy barrier of the molecule.[79] To limit anti-cooperative effects associated with direct lateral interactions and to exclude a contribution from Co clusters on graphene, we performed a vibrational investigation on the bi-metallic layer with a less-than stoichiometric amount of cobalt (namely a MnTPyP : Co = 0.6 ML : 0.2 ML). Trivially, the amount of adsorbed CO on MnTPyP–Co/Gr/Ir(111) increases with CO pressure, as it is determined by the stationary equilibrium between adsorption and desorption. The CO stretching region in the 1860–2040 cm^{-1} range was monitored *in situ* at room temperature as a function of the increasing CO pressure, from UHV to 0.1 mbar. The uptake data are plotted in Fig. 4, where the measured SFG intensity (color scale) is displayed as a function of both IR wavenumber and CO background pressure. The UHV spectrum is completely flat, but already above 5×10^{-7} mbar a weak signal starts to be detectable at 1942 cm^{-1}, progressively increasing with pressure, associated with the CO hot-band. A second resonance starts growing at 1968 cm^{-1} above 10^{-6} mbar with a phase that evolves with the CO pressure. Concerning the resonant amplitudes, we recall that the hot-band of CO on Ru(0001) and Ir(111) was observed by means of broadband SFG,[74,75] at variance with our case. The impinging IR beam spectrum was several hundreds of cm^{-1} broad; thus, the hot-band could be resonantly excited by the absorption of two photons of different energy, resonant with both $0 \rightarrow 1$ and $1 \rightarrow 2$ transitions, respectively. SFG spectra obtained in this way yield a more authentic representation of the population ratio between the ground and first excited vibrational levels. Instead, in a scanning-IR SFG configuration, the system is excited by a narrow IR pulse (less than 1 cm^{-1} width). The ideal way to study the hot-band in a scanning configuration would be to resonantly excite the fundamental transition with a fixed-wavelength IR pulse, while performing the SFG measurement using a second IR beam. In our case, at each point of the spectrum, the system is pumped and probed by the same scanning IR wavelength, so that the $0 \rightarrow 1$ and $1 \rightarrow 2$ transitions are excited by IR photons with the same energy. The hot-band is populated and detectable just because of the intrinsic broad linewidth of the partially overlapping resonances. Due to this reason, an independent, quantitative analysis of the single hot and fundamental resonances would not be physically meaningful, as it is not possible to disentangle the contribution of the different factors. For this reason, we tracked the evolution of the sum of the resonant signals, keeping in mind that the

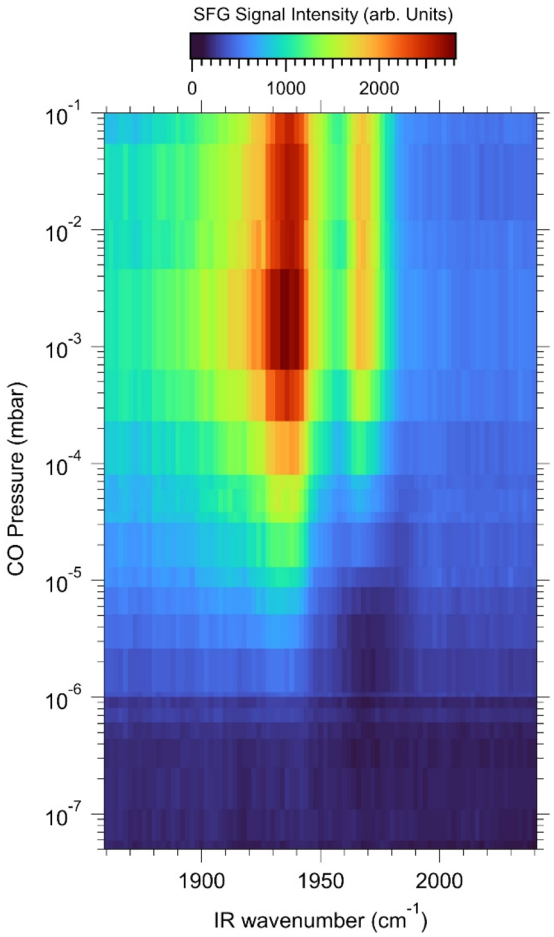

Fig. 4 IR-Vis SFG intensity map (color scale) as a function of the IR wavenumber and of the background CO pressure spanning over 7 orders of magnitude, measured at equilibrium and at room temperature in ppp polarization combination.

signal amplitude is proportional to the state population (coverage). To simplify the model and obtain some physical insight, the spectra imaged in Fig. 4 were fitted with globally optimized widths and phases. For the fundamental resonance we obtain $\Gamma_{0\to1} = 8.7 \pm 0.2$ cm^{-1} and $\omega_{0\to1} = 1968.2 \pm 0.3$ cm^{-1}, while for the hot-band we get $\Gamma_{1\to2} = 13.6 \pm 0.2$ cm^{-1} and $\omega_{1\to2} = 1942.0 \pm 0.2$ cm^{-1}. The hot-band wavenumber was kept fixed for all spectra acquired at pressure values lower than 10^{-6} mbar, as the low resonant amplitude makes the fit statistically unreliable in that region. The hot-band position was then left free to vary for increasing pressure above 10^{-6} mbar, oscillating around 1942.0 cm^{-1}, while the fundamental line position was globally fitted. The uptake profile obtained from the best fit of the data plotted in Fig. 4 is reported in Fig. 5 (markers, the shaded area delimits the experimental uncertainty). We can readily identify the saturation pressure to be around 10^{-3}–10^{-2} mbar, thus justifying the choice to perform the former AP-XPS investigation at 10^{-2} (Fig. 1) to assure that saturation of the available active metal centers was achieved. The uptake profile is best fitted with two different models, namely the Temkin isotherm and the Hill equation (black and blue lines in Fig. 5).[80–83] They are both extensively adopted in catalysis, biochemistry and pharmacology to (i) model the pressure-dependent saturation and retrieve the adsorption energy of a ligand to a receptor (Temkin), and (ii) to identify the cooperativity level of adjacent sites participating in the adsorption process (Hill). Specifically, we can evaluate the adsorption energy of CO on MnTPyP–Co by using the Temkin isotherm, an extended version of the Langmuir isotherm. The model has been largely misused and cited in its dimensionally inconsistent form in the literature. Recently, significant effort has been made to clarify this issue and recover its correct form and approximations.[82,83] We adopt here the following expression, already employed to describe adsorption on metal porphyrins:[84]

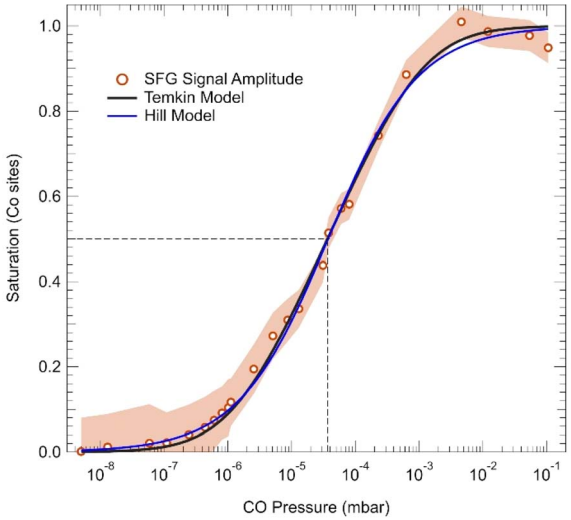

Fig. 5 CO saturation curve obtained from the evolution of the IR-Vis SFG amplitude of the C–O internal stretch resonances (markers) extracted from the best fit of the data reported in Fig. 4. The shaded area indicates the associated confidence interval (3σ). The continuous lines depict the best fit of the saturation curve according to the Hill (blue) and Temkin (black) models, respectively (see text for details). The dashed lines show the half-saturation values ($p_{0.5}$).

$$E_{ads}(\theta) = E^0_{ads}\left(1 + \alpha_T \frac{\theta}{\theta_{sat}}\right)$$

where $E_{ads}(\theta)$ is the coverage-dependent adsorption heat, E^0_{ads} a is the initial adsorption heat (formally the non-cooperative limit, which corresponds to the zero-coverage limit), α_T is the Temkin parameter, θ and θ_{sat} are the coverage and saturation coverage, respectively. The approximation of a linear adsorption heat dependence on θ reflects the degree of (anti)-cooperativity of the process, with α_T assuming values < 0 (anti-cooperativity), = 0 (no cooperativity), or >0 (cooperativity). In the SFG experiment, we get the evolution of the saturation (coverage) parameter from the resonant amplitude normalized to the saturation amplitude of the C–O internal stretch resonance as a measure of the θ/θ_{sat} term. The Hill equation provides complementary information about the degree of cooperativity between the adsorption sites.[81] More than one century ago, the model was originally exploited by Hill to describe the cooperative binding

of oxygen to hemoglobin,[21] relating the number of occupied receptors to the available ligand concentration by:

$$\frac{\theta}{\theta_{sat}} = \frac{p^n}{{p_{0.5}}^n + p^n}$$

where θ/θ_{sat} represents the ratio between occupied and total available binding sites, p is the gas pressure, $p_{0.5}$ is the pressure at which half of the total receptors are occupied, and n is the Hill coefficient.[81] The latter can assume only positive values, larger or smaller than 1, corresponding to cooperative and anti-cooperative binding, respectively. The $n = 1$ case indicates a non-cooperative response, meaning that adsorption on a certain site is not influenced by the occupation of neighboring sites. We also recall that both Temkin and Hill models reproduce the non-cooperative Langmuir isotherm, for $\alpha_T = 0$ and $n = 1$, respectively. Both fit curves in Fig. 5 look similar and are in excellent agreement with the experimental data. We obtain the following best values: $E^0_{ads} = 0.73 \pm 0.01$ eV, $\alpha_T = -0.11 \pm 0.02$, $p_{0.5} = (3.7 \pm 0.4) \times 10^{-5}$ mbar, and $n = 0.62 \pm 0.05$, which clearly indicate an anti-cooperative adsorption mechanism. The value found for E^0_{ads} indicates weak binding (the adsorption energy of CO/Ir(111) is 1.4–1.9 eV),[85] accounting for the observed reversibility of ligation at room temperature. In the case of CoTPyP–Co, coverage-dependent results were obtained for low and high Co loadings,[26] with ligation starting from 5×10^{-6} mbar CO and reaching saturation at 5×10^{-4} mbar. The minimum pressure at which CO was observed is almost 1 order of magnitude higher than for the MnTPyP–Co, and the saturation pressure was instead about half an order of magnitude lower, indicating a narrower uptake window despite the similar E^0_{ads}. This leads to the conclusion that while CO ligates to the same Co(I) peripheral sites on both M_1TPyP–Co/Gr/Ir(111) with M_1 = Mn, Co, M_1 plays a role in the kinetics of the uptake. For the present M_1 = Mn system, we observe anti-cooperativity ($n < 1$; $\alpha_T < 0$) despite the long distance (∼nm) between the nearest Co sites in the network, excluding the role of direct lateral interactions, as discussed for the M_1 = Co case.[26] The distinct anti-cooperative behavior ($\alpha_T = -0.11$) in the Mn–Co system, compared to pure Co–Co networks, stems from the central Mn center acting as an electronic 'buffer'. In this bimetallic configuration, the Mn–pyridyl interface is more sensitive to the electronic footprint of the CO–Co bond, thereby regulating the degree of π-backdonation at neighboring sites. Several mechanisms have been proposed in the literature to explain similar effects for CO adsorption on Ir(111),[74] Pt(111),[65,86] Ru(0001),[66,75,87,88] and finally CoTPyP–Co/Gr/Ir(111).[26] Starting from the bare metal surfaces, blueshifts of the order of 30–80 cm^{-1} of the fundamental CO resonance are observed along the uptakes at RT, explained by CO dipole–dipole coupling between adjacent molecules, which are only a few Å distant, whereas on the MnTPyP–Co system the minimum distance between neighboring adsorption sites is ∼1.4 nm (with second-nearest-neighbors at ∼2 nm and third-nearest-neighbors at ∼2.8 nm), making the direct lateral interaction between the ligands completely negligible, as demonstrated for CO/FePc,[23] and CO/CoTPyP–Co.[26] Indeed, the direct dipole–dipole interaction potential energy can be written in the form:

$$U(r) = \frac{{d_{CO}}^2}{4\pi\varepsilon_0 r^3}$$

where r is the distance between the dipoles (d_{CO}), and ε_0 the vacuum permittivity. By setting $r = 1.4$ nm and $d_{CO} = 0.112$ D,[23,26] the resulting interaction energy is $U = 3 \times 10^{-6}$ eV, corresponding to a wavenumber blue-shift of the order of 0.02 cm^{-1}. Thus, we can safely discard the dipole–dipole coupling hypothesis as a candidate explanation for the observed anti-cooperativity. Alternatively, as for other cases, we can consider the effects originating from the vibrational energy delocalization by means of a Förster resonance energy transfer process,[74,87] the indirect interaction between the metal centers mediated by the organic backbone,[26] or by the underlying surface through the *trans*-effect. According to the Förster's model, an excited oscillator can exchange vibrational energy with an unexcited one, by means of dipole–dipole coupling.[89,90] The local-oscillator behavior of CO on Ru(001) has a breakdown at around 0.33 ML, due to the strong dipole–dipole coupling among adsorbates and the resulting vibrational energy delocalization,[87] similarly to the case of CO/Ir(111).[74] As a consequence, the hot-band is quenched while the fundamental gets broader for increasing CO coverage, which is not compatible with our data. Furthermore, we already demonstrated above that in our case dipole–dipole interactions are negligible. We can thus rule out this mechanism as well. In the similar CoTPyP–Co/Gr system, the origin of the cooperativity was attributed to the heterostructure itself, by means of charge transfer and distortion of the organic backbone induced by carbonylation,[26] together with the network-mediated magnetic coupling of the metal sites, as predicted by Mandal *et al.*[91] This latter explanation is compatible with our case, where we witness a relevant evolution with the CO coverage of the two resonances at 1594 and 1616 cm^{-1} (Fig. S6), assigned to stretching and δ modes of the pyridyl moieties, respectively. While the line positions remain unaltered from UHV to 0.01 mbar CO (saturation), we observe a non-resonant background increase of about 15%, accompanied by a phase rotation of the resonances, related to a ligand-induced electronic structure change of the layer, in agreement with the charge redistribution evidenced by our present *ab initio* DFT calculations and our previous studies on a similar system.[26]

Concerning the CO ligation geometry, we further investigated this aspect by measuring the internal C–O stretching region in both ppp and ssp polarization combinations as a function of the gas pressure. The two measurements sample different components of the non-linear susceptibility tensor,[92] thus providing indirect information on the dipole spatial orientation.[72] As shown in Fig. 3a and b, the spectra were fitted by globally optimizing line positions and widths, letting only amplitudes and phases to vary. The ssp signal is overall less intense (by about one order of magnitude) than the ppp counterpart. The straightforward information that we can extract is that the CO ligand is not standing completely upright at the Co sites but is slightly tilted, as confirmed by our computational insight. However, the I_{ppp}/I_{ssp} ratio is determined not only by the contribution of the ligand adsorption angle, but also from

electronic effects through the ratio between the hyperpolarizability factors,[7] making it reasonable to associate the huge discrepancy observed for the relative intensities of the fundamental and hot bands to different hyperpolarizabilities, rather than to a completely different adsorption geometry of the excited state, considering that the electronic transition moment is the most affected by the change of the Vis and SFG polarization from p to s.

Conclusions

We have shown that carbon monoxide ligates selectively to Co(I) single metal atom sites in a manganese–cobalt coordination network that we obtain by self-assembly on a single graphene sheet. Adsorption is fully reversible and pressure-dependent, with saturation occurring above 10^{-3} mbar at room temperature. Spectroscopic and computational analyses confirm weak Co–CO bonding, with population of both fundamental and hot-band excitations of the CO stretch mode upon irradiation with infrared photons. The uptake behavior is well modeled by Temkin and Hill isotherms, showing anti-cooperative adsorption. The latter property is not due to direct dipole–dipole interactions but likely arises from electronic and magnetic effects mediated by the molecular network. Our findings offer insight into ligand dynamics at single metal atom sites and highlight the potential of surface-confined metal–organic networks for tunable reactivity under ambient conditions, with implications for catalysis and molecular sensing. This same approach can be adopted at a fundamental level to investigate experimentally the reactivity properties of single metal atoms sites in 2D materials at surfaces throughout an extended pressure range, from UHV to the mbar range, despite the extremely low surface concentration of the reactive sites. With specific reference to the M_1TPyP–M_2 system,[91] several $M_{1,2}$ combinations could be configured, including not only 1,2 = Co, Mn, but also Fe, * (empty site), Cu, Pd, Ni *etc.*

Author contributions

E. V. conceived and designed the project. M. D. C., D. C., S. B., A. N. and D. B. conducted the experiments. M. S. provided fundamental assistance at the beamline. B. R., and P. G performed the theoretical calculations. A. N., M. D. C., B. R., and E. V. discussed all results and edited the manuscript. M. D. C., D. C., and S. B. contributed equally to the experimental work. All authors have reviewed and contributed to the published version of the manuscript.

Conflicts of interest

There are no conflicts to declare.

Data availability

Additional experimental and computational data supporting this article have been included as part of the supplementary information (SI). Further data is available from the corresponding authors upon reasonable request.

Supplementary information is available. See DOI: https://doi.org/10.1039/d5ta10405j.

Acknowledgements

This work was funded by Unione Europea – Next Generation EU through project PRIN2022 XXJNRS 2DOrNotToBe CUP J53D23001510006 and Next Generation EU, Missione 4 Componente 1 CUP J53D23016180001 PRIN PNRR P2022B3WCB 2Dgo3D. We acknowledge MAX IV Laboratory for time on Beamline HIPPIE under Proposals 20220031, 20220898 and 20221030. Research conducted at MAX IV, a Swedish national user facility, is supported by the Swedish Research council under contract 2018-07152, the Swedish Governmental Agency for Innovation Systems under contract 2018-04969, and Formas under contract 2019-02496. PG acknowledges ISCRA for access to the LEONARDO supercomputer, owned by the EuroHPC Joint Undertaking, hosted by CINECA (Italy).

Notes and references

1 S. S. Sung and R. Hoffmann, *J. Am. Chem. Soc.*, 1985, **107**, 578–584.
2 K. Gotterbarm, C. Bronnbauer, U. Bauer, C. Papp and H. Steinru, *J. Phys. Chem. C*, 2014, **118**, 25097–25103.
3 A. Tuxen, S. Carenco, M. Chintapalli, C.-H. Chuang, C. Escudero, E. Pach, P. Jiang, F. Borondics, B. Beberwyck, a P. Alivisatos, G. Thornton, W.-F. Pong, J. Guo, R. Perez, F. Besenbacher and M. Salmeron, *J. Am. Chem. Soc.*, 2013, **135**, 2273–2278.
4 N. Podda, M. Corva, F. Mohamed, Z. Feng, C. Dri, F. Dvorák, V. Matolin, G. Comelli, M. Peressi, E. Vesselli, F. Dvorak, V. Matolín, G. Comelli, M. Peressi and E. Vesselli, *ACS Nano*, 2017, **11**, 1041–1053.
5 J. Hulva, M. Meier, R. Bliem, Z. Jakub, F. Kraushofer, M. Schmid, U. Diebold, C. Franchini and G. S. Parkinson, *Science*, 2021, **371**, 375–379.
6 X. Li, V. Pramhaas, C. Rameshan, P. Blaha and G. Rupprechter, *J. Phys. Chem. C*, 2020, **124**, 18102–18111.
7 X. Li, M. Roiaz, V. Pramhaas, C. Rameshan and G. Rupprechter, *Top. Catal.*, 2018, **61**, 751–762.
8 G. Rupprechter, T. Dellwig, H. Unterhalt and H.-J. Freund, *J. Phys. Chem. B*, 2001, **105**, 3797–3802.
9 K. Peters, C. Walker, P. Steadman, O. Robach, H. Isern and S. Ferrer, *Phys. Rev. Lett.*, 2001, **86**, 5325–5328.
10 L. Lukashuk, N. Yigit, R. Rameshan, E. Kolar, D. Teschner, M. Hävecker, A. Knop-Gericke, R. Schlögl, K. Föttinger and G. Rupprechter, *ACS Catal.*, 2018, **8**, 8630–8641.
11 M. Bonn, S. Funk, Ch. Hess, D. N. Denzler, C. Stampfl, M. Scheffler, M. Wolf and G. Ertl, *Science*, 1999, **285**, 1042–1045.
12 M. Dell'Angela, T. Anniyev, M. Beye, R. Coffee, A. Föhlisch, J. Gladh, T. Katayama, S. Kaya, O. Krupin, J. LaRue, A. Møgelhøj, D. Nordlund, J. K. Nørskov, H. Öberg, H. Ogasawara, H. Öström, L. G. M. Pettersson,

W. F. Schlotter, J. A. Sellberg, F. Sorgenfrei, J. J. Turner, M. Wolf, W. Wurth and A. Nilsson, *Science*, 2013, **339**, 1302–1305.

13 M. Beye, T. Anniyev, R. Coffee, M. Dell'Angela, A. Föhlisch, J. Gladh, T. Katayama, S. Kaya, O. Krupin, A. Møgelhøj, A. Nilsson, D. Nordlund, J. K. Nørskov, H. Öberg, H. Ogasawara, L. G. M. Pettersson, W. F. Schlotter, J. A. Sellberg, F. Sorgenfrei, J. J. Turner, M. Wolf, W. Wurth and H. Öström, *Phys. Rev. Lett.*, 2013, **110**, 186101.

14 H. Xin, J. LaRue, H. Öberg, M. Beye, M. Dell'Angela, J. J. Turner, J. Gladh, M. L. Ng, J. A. Sellberg, S. Kaya, G. Mercurio, F. Hieke, D. Nordlund, W. F. Schlotter, G. L. Dakovski, M. P. Minitti, A. Föhlisch, M. Wolf, W. Wurth, H. Ogasawara, J. K. Nørskov, H. Öström, L. G. M. Pettersson, A. Nilsson and F. Abild-Pedersen, *Phys. Rev. Lett.*, 2015, **114**, 156101.

15 H. Öström, H. Öberg, H. Xin, J. LaRue, M. Beye, M. Dell'Angela, J. Gladh, M. L. Ng, J. A. Sellberg, S. Kaya, G. Mercurio, D. Nordlund, M. Hantschmann, F. Hieke, D. Kühn, W. F. Schlotter, G. L. Dakovski, J. J. Turner, M. P. Minitti, A. Mitra, S. P. Moeller, A. Föhlisch, M. Wolf, W. Wurth, M. Persson, J. K. Nørskov, F. Abild-Pedersen, H. Ogasawara, L. G. M. Pettersson and A. Nilsson, *Science*, 2015, **347**, 978–982.

16 N. Okabayashi, T. Frederiksen, A. Liebig and F. J. Giessibl, *Phys. Rev. B*, 2023, **108**, 165401.

17 S. Wu, *Science*, 2020, **367**, 148–149.

18 A. Choudhury, J. A. DeVine, S. Sinha, J. A. Lau, A. Kandratsenka, D. Schwarzer, P. Saalfrank and A. M. Wodtke, *Nature*, 2022, **612**, 691–695.

19 J. A. Lau, L. Chen, A. Choudhury, D. Schwarzer, V. B. Verma and A. M. Wodtke, *Nature*, 2021, **589**, 391–395.

20 B. H. McMahon, B. P. Stojković, P. J. Hay, R. L. Martin and A. E. García, *J. Chem. Phys.*, 2000, **113**, 6831.

21 A. V. Hill, *Biochem. J.*, 1913, **7**, 471–480.

22 K. Seufert, W. Auwärter and J. V. Barth, *J. Am. Chem. Soc.*, 2010, **132**, 18141–18146.

23 M. Corva, A. Ferrari, M. Rinaldi, Z. Feng, M. Roiaz, C. Rameshan, G. Rupprechter, R. Costantini, M. Dell'Angela, G. Pastore, G. Comelli, N. Seriani and E. Vesselli, *Nat. Commun.*, 2018, **9**, 4703.

24 M. Corva and E. Vesselli, *J. Phys. Chem. C*, 2016, **120**, 22298–22303.

25 M. Corva, F. Mohamed, E. Tomsic, Z. Feng, T. Skala, G. Comelli, N. Seriani, M. Peressi, E. Vesselli, T. Skála, G. Comelli, N. Seriani, M. Peressi and E. Vesselli, *ACS Nano*, 2018, **12**, 10755–10763.

26 F. Armillotta, A. Sala and E. Vesselli, *J. Phys. Chem. C*, 2024, **128**, 15613–15623.

27 R. Jose, S. Pal and G. Rajaraman, *Chem. Commun.*, 2023, **59**, 10315–10318.

28 F. Armillotta, D. Bidoggia, S. Baronio, P. Biasin, A. Annese, M. Scardamaglia, S. Zhu, B. Bozzini, S. Modesti, M. Peressi and E. Vesselli, *ACS Catal.*, 2022, 7950–7959.

29 W. Hieringer, K. Flechtner, A. Kretschmann, K. Seufert, W. Auwärter, J. V. Barth, A. Görling, H.-P. Steinrück and J. M. Gottfried, *J. Am. Chem. Soc.*, 2011, **133**, 6206–6222.

30 S. Baronio, M. De Col, A. Yadav, B. Roondhe, V. Mischke, O. Resel, D. Bidoggia, A. Namar, N. Vinogradov, M. Scardamaglia, M. Valvidares, P. Gargiani, M. Cinchetti, G. Zamborlini, P. Giannozzi and E. Vesselli, *Nanoscale*, 2025, **17**, 16946–16963.

31 J. P. Beggan, S. A. Krasnikov, N. N. Sergeeva, M. O. Senge and A. A. Cafolla, *Nanotechnology*, 2012, **23**, 235606.

32 S. R. Alharbi, A. A. A. Darwish, S. E. A. Garni, H. I. ElSaeedy and K. F. A. El-Rahman, *Infrared Phys. Technol.*, 2016, **78**, 77–83.

33 A. A. Attia, A. M. A. El-Barry, E. A. A. EL-Shazly and L. M. D. El-Deen, *J. Lumin.*, 2018, **199**, 391–399.

34 B. E. Murphy, S. A. Krasnikov, N. N. Sergeeva, A. A. Cafolla, A. B. Preobrajenski, A. N. Chaika, O. Lübben and I. V. Shvets, *ACS Nano*, 2014, **8**, 5190–5198.

35 G. Kyriakou, M. B. Boucher, A. D. Jewell, E. A. Lewis, T. J. Lawton, A. E. Baber, H. L. Tierney, M. Flytzani-Stephanopoulos and E. C. H. Sykes, *Science*, 2012, **335**, 1209–1212.

36 A. Yadav, S. Baronio, M. De Col, D. Comini, V. Mischke, A. Namar, N. A. Vinogradov, M. Scardamaglia, M. Cinchetti, G. Zamborlini, P. Giannozzi and E. Vesselli, *Nanoscale*, 2026, DOI: 10.1039/D5NR04824A.

37 F. Armillotta, D. Bidoggia, S. Baronio, A. Sala, R. Costantini, M. dell'Angela, I. Cojocariu, V. Feyer, A. Morgante, M. Peressi and E. Vesselli, *Adv. Funct. Mater.*, 2024, **34**, 2408200.

38 C. S. Tian and Y. R. Shen, *Surf. Sci. Rep.*, 2014, **69**, 105–131.

39 Y. R. Shen, *Nature*, 1989, **337**, 519–525.

40 M. Corva, Z. Feng, C. Dri, F. Salvador, P. Bertoch, G. Comelli and E. Vesselli, *Phys. Chem. Chem. Phys.*, 2016, **18**, 6763–6772.

41 M. Corva, F. Mohamed, E. Tomsic, M. Rinaldi, C. Cepek, N. Seriani, M. Peressi and E. Vesselli, *J. Phys. Chem. C*, 2019, **123**, 3916–3922.

42 M. Bonn, C. Hess, W. G. Roeterdink, H. Ueba and M. Wolf, *Chem. Phys. Lett.*, 2004, **388**, 269–273.

43 B. Busson and A. Tadjeddine, *J. Phys. Chem. C*, 2009, **113**, 21895–21902.

44 S. Zhu, M. Scardamaglia, J. Kundsen, R. Sankari, H. Tarawneh, R. Temperton, L. Pickworth, F. Cavalca, C. Wang, H. Tissot, J. Weissenrieder, B. Hagman, J. Gustafson, S. Kaya, F. Lindgren, I. Källquist, J. Maibach, M. Hahlin, V. Boix, T. Gallo, F. Rehman, G. D'Acunto, J. Schnadt and A. Shavorskiy, *J. Synchrotron Radiat.*, 2021, **28**, 624–636.

45 S. Doniach and M. Sunjic, *J. Phys. C Solid State Phys.*, 1970, **3**, 285–291.

46 P. Giannozzi, S. Baroni, N. Bonini, M. Calandra, R. Car, C. Cavazzoni, D. Ceresoli, G. L. Chiarotti, M. Cococcioni, I. Dabo, A. Dal Corso, S. de Gironcoli, S. Fabris, G. Fratesi, R. Gebauer, U. Gerstmann, C. Gougoussis, A. Kokalj, M. Lazzeri, L. Martin-Samos, N. Marzari, F. Mauri, R. Mazzarello, S. Paolini, A. Pasquarello, L. Paulatto, C. Sbraccia, S. Scandolo, G. Sclauzero, A. P. Seitsonen, A. Smogunov, P. Umari and R. M. Wentzcovitch, *J. Phys.:Condens. Matter*, 2009, **21**, 395502.

47 P. Giannozzi, O. Andreussi, T. Brumme, O. Bunau, M. Buongiorno Nardelli, M. Calandra, R. Car, C. Cavazzoni, D. Ceresoli, M. Cococcioni, N. Colonna, I. Carnimeo, A. Dal Corso, S. de Gironcoli, P. Delugas, R. A. DiStasio, A. Ferretti, A. Floris, G. Fratesi, G. Fugallo, R. Gebauer, U. Gerstmann, F. Giustino, T. Gorni, J. Jia, M. Kawamura, H.-Y. Ko, A. Kokalj, E. Küçükbenli, M. Lazzeri, M. Marsili, N. Marzari, F. Mauri, N. L. Nguyen, H.-V. Nguyen, A. Otero-de-la-Roza, L. Paulatto, S. Poncé, D. Rocca, R. Sabatini, B. Santra, M. Schlipf, A. P. Seitsonen, A. Smogunov, I. Timrov, T. Thonhauser, P. Umari, N. Vast, X. Wu and S. Baroni, *J. Phys.:Condens. Matter*, 2017, **29**, 465901.
48 D. Bidoggia, F. Armillotta, A. Sala, E. Vesselli and M. Peressi, *J. Phys. Chem. C*, 2024, **128**, 1737–1745.
49 J. P. Perdew, K. Burke and M. Ernzerhof, *Phys. Rev. Lett.*, 1996, **77**, 3865–3868.
50 M. Cococcioni and S. de Gironcoli, *Phys. Rev. B:Condens. Matter Mater. Phys.*, 2005, **71**, 035105.
51 S. Grimme, J. Antony, S. Ehrlich and H. Krieg, *J. Chem. Phys.*, 2010, **132**, 154104.
52 D. Vanderbilt, *Phys. Rev. B:Condens. Matter Mater. Phys.*, 1990, **41**, 7892–7895.
53 K. F. Garrity, J. W. Bennett, K. M. Rabe and D. Vanderbilt, *Comput. Mater. Sci.*, 2014, **81**, 446–452.
54 M. Methfessel and A. T. Paxton, *Phys. Rev. B:Condens. Matter Mater. Phys.*, 1989, **40**, 3616–3621.
55 R. Fletcher, *Practical Methods of Optimization*, Wiley, Chichester ; New York, 2nd edn, 1987.
56 H. J. Monkhorst and J. D. Pack, *Phys. Rev. B*, 1976, **13**, 5188–5192.
57 R. F. W. Bader, *Acc. Chem. Res.*, 1985, **18**, 9–15.
58 P. H.-L. Sit, R. Car, M. H. Cohen and A. Selloni, *Inorg. Chem.*, 2011, **50**, 10259–10267.
59 B. Eren and A. R. Head, *J. Phys. Chem. C*, 2020, **124**, 3557–3563.
60 C. R. O'Connor, J. A. Boscoboinik, M. Karatok and M. A. Van Spronsen, *Surf. Sci. Spectra*, 2020, **27**, 014002.
61 M. Scardamaglia, T. Susi, C. Struzzi, R. Snyders, G. Di Santo, L. Petaccia and C. Bittencourt, *Sci. Rep.*, 2017, **7**, 1–11.
62 J. Lahtinen, J. Vaari and K. Kauraala, *Surf. Sci.*, 1998, **418**, 502–510.
63 Y. He, C. J. Weststrate, D. Luo, J. W. Niemantsverdriet, K. Wu, J. Xu, Y. Yang, Y. Li and X. Wen, *Appl. Surf. Sci.*, 2021, **569**, 151045.
64 B. Eren, C. Heine, H. Bluhm, G. A. Somorjai and M. Salmeron, *J. Am. Chem. Soc.*, 2015, **137**, 11186–11190.
65 H. Aizawa and S. Tsuneyuki, *Surf. Sci.*, 1998, **399**, L364–L370.
66 H. Pfnür, D. Menzel, F. M. Hoffmann, A. Ortega and A. M. Bradshaw, *Surf. Sci.*, 1980, **93**, 431–452.
67 M. A. Ribeiro, M. Lanznaster, M. M. P. Silva, J. A. L. C. Resende, M. V. B. Pinheiro, K. Krambrock, H. O. Stumpf and C. B. Pinheiro, *Dalton Trans.*, 2013, **42**, 5462.
68 G. Blyholder, *J. Phys. Chem.*, 1964, **68**, 2772–2777.
69 A. A. Khassin, T. M. Yurieva, V. V. Kaichev, V. I. Bukhtiyarov, A. A. Budneva, E. A. Paukshtis and V. N. Parmon, *J. Mol. Catal. A:Chem.*, 2001, **175**, 189–204.
70 K. Sato, Y. Inoue, I. Kojima, E. Miyazaki and I. Yasumori, *J. Chem. Soc. Faraday Trans. 1 Phys. Chem. Condens. Phases*, 1984, **80**, 841.
71 Y. Yao, L. Chen, X. Mao, Y. Yang, J. Chen and L. Zhou, *J. Phys. Chem. C*, 2021, **125**, 8606–8619.
72 X. Li, S. Baronio, S. Gross, T. Haunold, E. Vesselli and G. Rupprechter, *J. Phys. Chem. C*, 2025, **129**, 12551–12560.
73 E. K. Plyler, L. R. Blaine and W. S. Connor, *J. Opt. Soc. Am.*, 1955, **45**, 102.
74 V. L. Zhang, H. Arnolds and D. A. King, *Surf. Sci.*, 2005, **587**, 102–109.
75 C. Hess, M. Bonn, S. Funk and M. Wolf, *Chem. Phys. Lett.*, 2000, **325**, 139–145.
76 I. Swart, A. Fielicke, D. M. Rayner, G. Meijer, B. M. Weckhuysen and F. M. F. de Groot, *Angew. Chem., Int. Ed.*, 2007, **46**, 5317–5320.
77 N. Mina-Camilde, C. Manzanares I. and J. F. Caballero, *J. Chem. Educ.*, 1996, **73**, 804.
78 D. H. Rank, A. H. Guenther, G. D. Saksena, J. N. Shearer and T. A. Wiggins, *J. Opt. Soc. Am.*, 1957, **47**, 686.
79 I. Morichika, K. Murata, A. Sakurai, K. Ishii and S. Ashihara, *Nat. Commun.*, 2019, **10**, 3893.
80 R. Gesztelyi, J. Zsuga, A. Kemeny-Beke, B. Varga, B. Juhasz, A. Tosaki and A. Hist, *Exact Sci.*, 2012, **66**, 427–438.
81 J. N. Weiss, *FASEB J.*, 1997, **11**, 835–841.
82 K. H. Chu, *Ind. Eng. Chem. Res.*, 2021, **60**, 13140–13147.
83 X. Zhou, R. Maimaitiniyazi and Y. Wang, *Arab. J. Chem.*, 2022, **15**, 104267.
84 K. N. Johnson, B. Chilukuri, Z. E. Fisher, K. W. Hipps and U. Mazur, *Curr. Org. Chem.*, 2022, **26**, 553–562.
85 F. Abild-Pedersen and M. P. Andersson, *Surf. Sci.*, 2007, **601**, 1747–1753.
86 A. Crossley and D. A. King, *Surf. Sci.*, 1977, **68**, 528–538.
87 Ch. Hess, M. Wolf and M. Bonn, *Phys. Rev. Lett.*, 2000, **85**, 4341–4344.
88 M. Bonn, C. Hess and M. Wolf, *J. Chem. Phys.*, 2001, **115**, 7725–7735.
89 G. D. Scholes, *Annu. Rev. Phys. Chem.*, 2003, **54**, 57–87.
90 Th. Förster, *Ann. Phys.*, 1948, **437**, 55–75.
91 B. Mandal, J. S. Chung and S. G. Kang, *J. Phys. Chem. C*, 2018, **122**, 9899–9908.
92 A. G. Lambert, P. B. Davies and D. J. Neivandt, *Appl. Spectrosc. Rev.*, 2005, **40**, 103–145.